



**Formation of nanocrystalline manganese oxide in flames:  
oxide phase governed by classical nucleation and size-  
dependent equilibria**

Journal:	<i>CrystEngComm</i>
Manuscript ID	CE-ART-05-2020-000734.R2
Article Type:	Paper
Date Submitted by the Author:	31-Jul-2020
Complete List of Authors:	Dasappa, Shruthi; San Diego State University, Mechanical Engineering; University of California San Diego, Camacho, Joaquin; San Diego State University, Mechanical Engineering Dept

SCHOLARONE™  
Manuscripts

## ARTICLE

Received 00th January 20xx,  
Accepted 00th January 20xx

DOI: 10.1039/x0xx00000x

## Formation of nanocrystalline manganese oxide in flames: oxide phase governed by classical nucleation and size-dependent equilibria

Shruthi Dasappa<sup>a,b</sup> and Joaquin Camacho <sup>\*a</sup>

Particle nucleation and growth of crystalline manganese oxide nanoparticles was examined in a complementary experimental and modelling study. Gas-to-particle conversion occurred in a flame-assisted chemical vapor deposition process whereby a premixed stagnation flame drove the high-temperature synthesis. The structure of the stagnation flame was computed using pseudo one-dimensional and axisymmetric two-dimensional methods to assess the accuracy of using a faster similarity-based calculation for flame-deposition design. The pseudo one-dimensional computation performs reasonably well for the narrow aspect ratio stagnation flow currently studied as evidenced by reasonable agreement between the measured flame position and both computational methods. Manganese oxide nanoparticles having II, II-III, III or IV oxidation states were observed depending on the flame conditions. These observations may be explained by size-dependent equilibria between nano-scale manganese oxide and surrounding gas-phase oxygen. Local equilibrium was assessed during the particle temperature-oxygen-time history to gain insight into oxide formation in the flame. Analysis of the saturation ratio for formation of condensed MnO in the flame indicates that nucleation may be limited by a thermodynamic barrier. This nucleation mechanism is supported by measured particle sizes smaller than what would be expected from a coagulation limited growth process. Nanocrystalline MnO, reported here for the first time by flame synthesis, was obtained in oxygen lean flames. MnO<sub>2</sub> is the phase predicted to be thermally stable as the particles approach the deposition surface, yet other metastable oxide phases were produced in many of the flames examined. In fact, MnO<sub>2</sub> was only observed in the smallest particle size conditions which may indicate that high cooling rates limit phase equilibrium to less massive particles.

<sup>a</sup> Mechanical Engineering Department, San Diego State University, San Diego, CA USA

<sup>b</sup> Mechanical and Aerospace Engineering Department, University of California San Diego, San Diego, CA, USA

† Footnotes relating to the title and/or authors should appear here.

Electronic Supplementary Information (ESI) available: [details of any supplementary information available should be included here]. See DOI: 10.1039/x0xx00000x

## Introduction

Manganese oxide nano-materials have been incorporated into many promising technologies including energy storage materials<sup>1,2</sup>, MRI contrast agents<sup>3,4</sup> and catalysts ( see e.g., NOx reduction<sup>5,6</sup>, Water Oxidation<sup>7</sup>). Flame made manganese oxide nano-materials, mostly produced by flame spray pyrolysis<sup>8–10</sup>, have been reported for a variety of applications. Manganese oxide nanoparticles produced by flame stabilized on a rotating surface (FSRS) was reported previously<sup>11</sup> and it was observed that either Mn<sub>3</sub>O<sub>4</sub>, Mn<sub>2</sub>O<sub>3</sub> or MnO<sub>2</sub> are formed depending on growth conditions in the premixed flame. This is in contrast to many titanium oxide and iron oxide premixed flames studies where full oxidation to TiO<sub>2</sub> and Fe<sub>2</sub>O<sub>3</sub> is reported. There are notable exceptions such as a recent report of TiO<sub>2</sub>-II formation in fuel rich FSRS conditions<sup>12</sup>. The current work is a complementary experimental and modelling study examining formation of nanocrystalline manganese oxides in flames with analysis of thermodynamic barriers to particle nucleation and oxidation.

Synthesis of manganese oxide nanoparticles will be carried out in a flame-assisted chemical vapor deposition process. The process is similar to previous FSRS reports<sup>12–14</sup> except that a stationary deposition surface is used rather than deposition onto a rotating substrate. The stationary deposition surface enables rigorous modelling of the CVD domain and examination of competing processes leading to the final oxide product. In the current work, manganese oxide nanoparticles are synthesized by gas-to-particle conversion driven by premixed stagnation flames with well-characterized flame structure and boundary conditions. Competing oxidation and growth mechanisms for manganese oxide will be examined in terms of systematic variation of the in-flame temperature-oxygen-time history.

The synthesis flame is a flat reaction zone with axisymmetric two-dimensional geometry similar to conventional CVD domains. As first outlined by Kee<sup>15</sup>, this type of flame structure could be solved using a similarity formulation in which the radial component is expressed in terms of the axial component. This pseudo one-dimensional approach could enable efficient yet powerful process design for material synthesis by simplifying the flow field and enabling detailed chemistry and physics to be incorporated. The similarity scaling of a linear dependence on  $r$  for radial velocity is most accurate for domains with a wide inlet boundary to stagnation boundary aspect ratio<sup>16,17</sup>. The aspect ratio of the burner to stagnation currently studied is relatively narrow as it is closer to some CVD geometries<sup>18</sup>. Solutions obtained using the pseudo one-dimensional (self-similar) formulation for the current aspect ratio will be compared to a separate computation of the two-dimensional axis-symmetric flame structure. The comparison between one and two-

dimensional flame computations will provide insight into efficient flame structure calculation for the narrow aspect ratio domain and relatively large flame standoff distance used here.

Formation of manganese oxide nanoparticles in flames is less understood than titanium oxide and iron oxide. Flame synthesis of titania has been carried out on the industrial scale for a century and academic studies exist going back decades. There is evidence that formation mechanisms for manganese oxides in flames may differ from those observed for titania. One example was discussed above in terms of the stable manganese oxides observed with a variation in oxidation states. A range of crystal phases has been reported for titanium oxide nanoparticles formed in flames<sup>12,14,19</sup> but the oxidation state observed was mostly Titanium(IV) oxide. This range of phases has been explained on the basis of shifts to bulk phase equilibrium driven by the surface energy of nanoparticles<sup>14,20</sup>. Birkner and Navrotsky assessed phase-stability for nano-scale manganese oxide under oxygen by drop-solution calorimetry for  $\text{MnO}_2$ ,  $\text{Mn}_2\text{O}_3$  and  $\text{Mn}_3\text{O}_4$  and surface energies were reported, respectively, as 2.05, 1.77 and 1.62 J/m<sup>2</sup>.<sup>21</sup> A phase stability diagram incorporating the surface energy effect is shown in Fig. 1 with an extension to the  $\text{MnO}$  phase<sup>22</sup> (1.13 J/m<sup>2</sup>). The flame synthesis process currently studied will encompass the entire range of size-temperature-oxygen space shown in the diagram. The size-dependent phase diagram will be a basis to assess the degree to which phase equilibrium is established among the nanocrystalline manganese oxides formed. In addition, the wide range of physical properties of the manganese oxides calls into question the validity of the coagulation limited nucleation mechanism adopted for flame synthesis of  $\text{TiO}_2$  nanoparticles. These considerations will be examined here by systematic observation of manganese oxide formed in a flame with a well-characterized temperature-oxygen-time history.

## Computational

Premixed stagnation flames on a stationary surface are modelled here using both a pseudo one-dimensional model and a full two-dimensional axisymmetric computation. The flame computations do not include particle precursor, nor do they consider nanoparticle synthesis processes in the flame. Rather, the flame structure resulting from the base ethylene-oxygen-argon mixture is calculated. An experimental comparison between flames with and without precursor doping is carried out below to assess the range, if any, for neglecting role of the Mn oxide precursor on the flame structure. Thermodynamic analysis of manganese oxide nucleation and phase stability, described below, is carried out after the structure of the base flame is computed. An objective of the study is to determine the accuracy of using the pseudo one-dimensional computation for material synthesis processes having geometry at the limits of the self-similar range.

The pseudo one-dimensional flame structure solution was obtained using OPPDIF<sup>23</sup> modified to include  $\text{CO}_2$  and  $\text{H}_2\text{O}$  radiation. The boundary conditions include the measured temperatures at the boundaries and the inlet flow rates. Plug

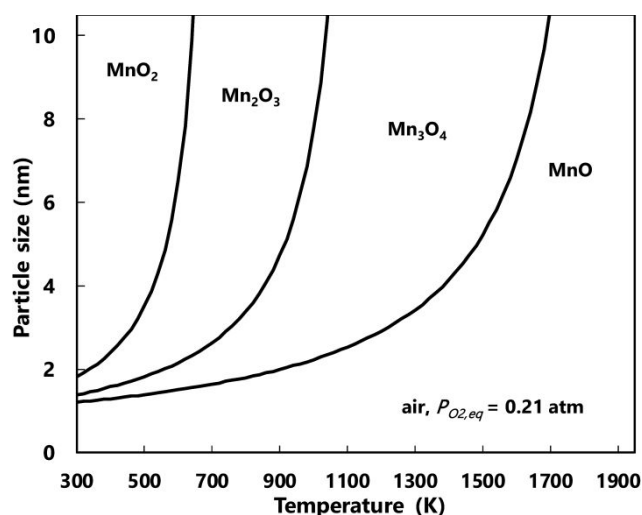


Figure 1 Phase stability diagram based on particle size for nano-scale manganese oxide under air.

flow (zero radial velocity) is assumed at the nozzle and diffusion of species is allowed into the nozzle boundary. The axial, radial and diffusive velocities are zero at the stagnation surface and the zero diffusive velocity for each gas-phase species is the result of counteracting Fickian and thermal diffusion processes. Windward differencing, the multicomponent transport formulation and thermal diffusion was considered within the Sandia CHEMKIN<sup>24</sup> framework for reacting flow problems. The two-dimensional axisymmetric computation also used CHEMKIN to evaluate the chemical kinetic, thermal and transport aspects of the reacting flow. The reaction kinetic model considered for both computations was USC Mech II<sup>25</sup>, which has been shown to calculate heat release rates and premixed stagnation flame structure more accurately than other foundational combustion mechanisms<sup>26,27</sup>.

The two-dimensional axisymmetric computation was carried out on ANSYS Workbench (v.19.2) incorporating Fluent and CHEMKIN. The governing equations for continuity, momentum, energy and species conservation were solved in the axial and radial directions using CHEMKIN-CFD invoked through Fluent. The axisymmetric domain is defined along the axis of the burner nozzle and the width and height of the domain is 7.0 and 2.54 cm, respectively, for all flames. The domain is a simple projection of flame configuration without consideration of confinement or entrainment effects. The nozzle is considered a boundary of the domain as a 0.5 cm slit normal to the centerline (for the 1 cm diameter nozzle). The  $\text{N}_2$  sheath flow channel is a 0.2 cm opening adjacent to the nozzle opening. The computational mesh is 40800 cells mostly concentrated within 4 cm of the axis (99%). The side faces of the domain are pressure outlets, the stagnation surface face is specified as a wall boundary. The nozzle and sheath openings are set as velocity inlets. The Fluent viscosity model is set to laminar and the CHEMKIN mechanism is uploaded into the species-transport module. Radiation is not considered but thermal diffusion and multicomponent transport are. The initial guess for iterations is based on the OPPDIF solution for temperature and flame position. During initialization, the

temperature, O, H and OH concentrations are applied to a thin region on the mesh where OPPDIF predicts the flame position to be.

For ease of computation, the two-dimensional solution was only obtained for a limited set of flames and OPPDIF was relied upon to determine the temperature-oxygen-time history for particle synthesis. The performance of both computations is assessed in terms of comparison to experimentally measured flame position as discussed below. An objective of the current study is to show that the pseudo one-dimensional formulation is an efficient process design tool for stagnation flames even in narrow domains. Manganese oxide has been produced in premixed flames with a variety of oxidation states<sup>11</sup> and characterization of the flame structure is important for elucidating the competing processes.

Manganese oxide nanoparticles are formed in the flame and deposited onto a stationary deposition surface. The precursor, methylcyclopentadienyl manganese tricarbonyl (MMT, Sigma-Aldrich), is sprayed into the fuel line in its initial liquid state, mixed with the unburned gas mixture and vaporized before leaving the fuel line. The gas-to-particle conversion is assumed to occur after the flame front which, in this case, is a flat plane at a steady distance from the deposition surface. The calculations of the flame structure described above enable rigorous definition of the particle trajectory as the precursor breaks down at the flame front and forms manganese oxide in the post-flame region. All the oxide formation and growth processes are assumed to occur after passing the flame front.

The reaction time,  $t$ , is considered to be the time for a Langrangian particle to traverse the location of the flame front (considered as position where the temperature inflects sharply upwards) to the location of the stagnation surface. The particles are transported to the deposition surface by following the streamlines and by an additional thermophoretic force in the vicinity of the deposition surface. Neglecting diffusive processes, the total velocity of the particle is the sum of the convective and thermophoretic velocities. The reaction time is calculated from the integral of  $dx/V$  over the region described above. See previous work for details on this computation.<sup>28,29</sup> The reaction time is considered to approximate the time for MMT precursor breakdown, Mn oxidation and particle nucleation / growth to occur before deposition. Examination of the relationship between the oxide product properties and the synthesis flame structure is expected to shed light on the competing oxidation, nucleation and growth time scales.

The mechanism for thermal decomposition of MMT precursor and subsequent formation of oxides is unknown and beyond the scope of this study. However, an analogous flame synthesis system, iron oxide from iron pentacarbonyl, guides our initial assumptions. Extensive modeling<sup>30,31</sup> and experimental<sup>32,33</sup> studies of conversion of iron pentacarbonyl indicated the metal oxidation process began from metallic iron. It is assumed the manganese tricarbonyl precursor used here also produces metallic Mn. If this assumption is valid, then it follows that MnO is the first oxide to form. Nucleation from the gas-phase is hypothesized to occur by condensation of MnO after oxidation of gas-phase manganese:



Equilibrium partial pressures over MnO(s) measured at high temperature by Knudsen effusion mass spectrometry have been reported<sup>34</sup> and the partial pressure of Mn gas was orders of magnitude higher than that of MnO. This is evidence that metallic manganese, Mn, is not the first to nucleate due to the higher volatility. In addition, MnO is the first oxidation state so the higher oxides are assumed to evolve from MnO particles in the flame. Equilibria among manganese oxides under molecular oxygen are known to behave as follows:



The thermodynamic barrier to nucleation from the gas phase is quantified by the saturation ratio,  $S$ , which compares the concentration of relevant species to the equilibrium concentrations. For nucleation of MnO, this is given by:

$$S_o = \frac{P_{\text{Mn}} P_{\text{O}_2}^{1/2}}{P_{\text{Mn,eq}} P_{\text{O}_2,eq}^{1/2}} \quad (5)$$

where  $P_{\text{Mn}}$  and  $P_{\text{O}_2}$  are the local partial pressure of the relevant components in the flame derived from the flame structure computation. Calculated equilibrium partial pressures,  $P_{\text{Mn,eq}}$  and  $P_{\text{O}_2,eq}$  are determined by high-temperature equilibria reported<sup>34</sup> for eq. 1.

Equilibria between the manganese oxides depends on local temperature and oxygen partial pressure. In addition, an additional surface energy effect has been shown to significantly shift oxidation-reduction equilibria between nano-scale transition metal oxides<sup>20,35</sup> as follows:

$$\Delta G_{R,nano} = \Delta G_{R,bulk} + \frac{6\gamma}{d} \left( \frac{bM_b}{\rho_b} \gamma_b - \frac{aM_a}{\rho_a} \gamma_a \right) \quad (6)$$

where  $\Delta G_R$  is the free energy of reaction for nano-scale and bulk processes,  $d$  is the particle diameter,  $b$  is the product stoichiometric coefficient,  $a$  is the reactant stoichiometric coefficient,  $M$  is the molecular weight,  $\rho$  is the mass density of the bulk oxide and  $\gamma$  is the surface energy of the oxide. Equation 6 is applied to the manganese oxide equilibrium reactions listed above with surface energy values listed above in the introduction section.

For a given temperature, the equilibrium oxygen partial pressure between two oxides of the same size could be determined from an equilibrium constant based on eq. 6. A saturation ratio could then be defined to describe the local oxygen partial pressure relative to the equilibrium oxygen partial pressure. Among the nano-scale manganese oxides the saturation ratio is defined as follows:

$$S_i = \frac{P_{O_2, flame}}{P_{O_2, eq, i}} \text{ for } i = 1, 2, 3 \quad (7)$$

where the  $i$  subscript denotes equilibria for the second, third and fourth manganese oxidation steps listed in eqs. 2-4. The equilibrium values calculated by eqs. 5-7 will be based on local temperatures along the computed flame spatial and time domains. The well-defined trajectory of the particle during formation in the flame allows for equilibrium conditions to be defined as the manganese oxide traverses the reaction zone.

## Experimental

Flame synthesis of manganese oxide nanoparticles is carried out in premixed stagnation flames with subsequent deposition onto a stationary surface. A diagram of the experimental setup is shown in Fig. 2. Liquid MMT is sprayed into the heated fuel line by gas-assisted nebulizer (Precision 500-75P, 10 micron droplet rating) driven by 1 lpm argon flow. The spray and the unburned gases are kept at 390 K to speed vaporization and prevent condensation at cold spots. The 2 sec residence time in the fuel line provides ample time for mixing and vaporization. A new contraction nozzle having inner contours taken from Bergthorson<sup>36</sup> and a relatively broad rim to minimize flame flashback is used here. The aluminum nozzle has a nozzle diameter  $D = 1.0$  cm and the wall thickness is 0.2 cm at the nozzle exit. A shroud of nitrogen issuing from a concentric channel surrounds the main mixture flow. Manganese oxide products are deposited from the flame onto a stationary aluminum substrate with the nozzle-to-stagnation separation kept at  $L = 2.54$  cm for all experiments. Fine wire, type K

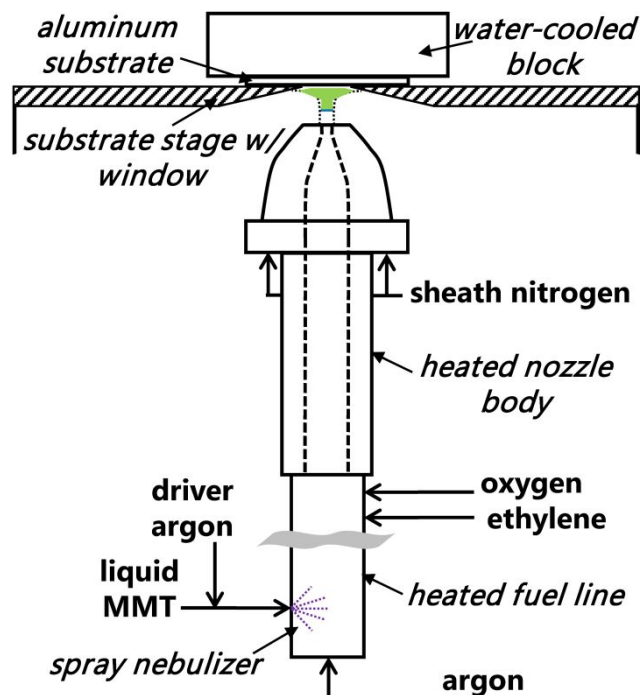


Figure 2 Experimental setup for the flame-assisted deposition process.

thermocouples are used to measure temperature of the unburned gas (nozzle boundary temperature) and the temperature at the deposition surface (stagnation boundary temperature). In the flame, the precursor (gas-phase MMT) decomposes, burns and the oxide product nucleates to form an aerosol.

Premixed stagnation flames provide high-temperature synthesis conditions with radial uniformity in thermal and chemical profiles<sup>37,38</sup>. In the current study, the flame structure is manipulated to give flame synthesis conditions with a desired temperature-oxygen-time history for particle growth. This can be achieved by proper balancing of the flow momentum and flame reactivity. For example, the strain rate was systematically decreased, in previous work, for a given unburned mixture to observe soot formation at increasing growth time<sup>26</sup>. The flame position is measured by analyzing the flame projection captured by DSLR camera as described previously.<sup>26,29</sup>

Table 1. Summary of flame synthesis conditions

Flame	$\phi$	$X_{Ar}$	$T_{f, max}$ (K)	$t$ (ms)	MMT (ppm)	Velocity, $v_o$ (cm/s)
A1	0.4	0.46	2600	4	200	335
A2	0.4	0.46	2600	4	300	335
A3	0.4	0.46	2600	4	500	335
B1	0.4	0.52	2510	4	100	301
B2	0.4	0.46	2600	4	100	335
B3	0.4	0.52	2510	4	200	301
B4	0.4	0.46	2600	4	200	335
B5	0.4	0.62	2315	7	500	252
B6	0.4	0.56	2450	6	500	290
B7	0.4	0.52	2510	4	500	301
B8	0.4	0.46	2600	4	500	335
C1	0.4	0.46	2600	4	100	335
C2	0.5	0.61	2560	5	100	299
C3	0.6	0.67	2590	5	100	305
C4	0.8	0.72	2620	5	100	316
D1	1.2	0.81	2390	7	200	267
D2	1.3	0.79	2480	6	200	279
D3	1.4	0.79	2400	7	200	269
D4	1.5	0.78	2390	6	200	279

Premixed ethylene-oxygen-argon laminar flames doped with MMT precursor are studied in the current work. A summary of the flame conditions studied is summarized in Table 1 in terms of experimental sets defined by flame temperature, reaction time and oxygen environment. A more detailed table is included in the supplemental material. Design of the experimental flame synthesis conditions was based on OPPDIF computations of the flame structure. Comparisons to experimental measurements of flame position and the two-dimensional computation will provide insight into the accuracy of OPPDIF for this nozzle-to-surface separation. Another assumption is that MMT precursor does not perturb the flame structure at the doping level considered here. With this in mind, the flame temperature, oxygen and time profiles assigned to

the experimental flames are determined by OPPDIF using measured boundary conditions.

The gas-phase oxygen levels during synthesis are characterized by the equivalence ratio,  $\Phi$ , of the unburned mixture. This is the ratio of inlet fuel to  $O_2$  over the stoichiometric fuel to  $O_2$  such that  $\Phi < 1$  corresponds to an oxygen-rich post-flame zone. For  $\Phi > 1$ , a small amount of oxygen remains after the flame and this approaches zero as  $\Phi \gg 1$ . The first set of experiments, labelled as the A series of flames, examines manganese oxide nanoparticle formation in the same oxygen-rich flame but at increasing levels of MMT precursor loading (Flames A1-A3). The inlet flow rate for flame A corresponds to a cold-gas-velocity of  $v_0 = 335$  cm/s and the mixture has  $\Phi = 0.4$  with argon mole fraction of  $X_{Ar} = 0.46$ . For  $L = 2.54$  cm with this inlet flow, OPPDIF predicts the maximum flame temperature as  $T_{f,max} = 2600$  K and  $t = 4$  ms. As reported previously<sup>11</sup>, the competition between manganese oxidation and particle growth is expected to be affected by precursor concentration for a given flame condition. The nanoparticle products are expected to form under the same temperature-oxygen-time history while undergoing different rates of particle growth. For series A flames, the precursor loading effect on synthesis products is isolated from temperature, oxygen and time effects.

The oxygen-rich condition ( $\Phi = 0.4$ ) is used again in the B series of flames to observe manganese oxide formation for a series of increasing flame temperature conditions ( $2340$  K  $< T_{f,max} < 2600$  K) all at comparable reaction time,  $t$  (Flames B1-B8). Precursor loadings of 100, 200 and 500 ppm are used in the B series to investigate competing growth and temperature effects. Comparable temperature and particle time is used in the C series to examine the role of gas-phase oxygen ( $0.4 < \Phi < 0.8$ ). Low MMT loading (100 ppm) is used to emphasize the role of gas-phase oxygen and the extent to which this limits oxidation. The D series further explores oxygen concentration effects by focusing on oxygen-lean growth conditions. This series of flames having  $1.2 < \Phi < 1.5$  is expected to produce lower oxidation states of manganese oxide.

Manganese oxide films deposited from the stagnation flame are characterized by off-line Raman spectroscopy, X-ray diffraction (XRD) and transmission electron microscopy (TEM). A Thermo DXR2 Raman Microscope with a 532 nm excitation source is used for spectra having Raman shifts spanning 300 to 3000  $cm^{-1}$ . The laser was focused under a 50x objective at 1 mW power. XRD measurements were carried out on a PANalytical X'pert Pro diffractometer equipped with a Cu X-ray tube operating at 45 kV and 40 mA. Counts were made for 1.5 sec for each 0.02 increment for  $20 < 2\theta < 60$ . The samples are transferred from the aluminum deposition substrate to glass for XRD analysis to avoid diffraction from aluminum. A FEC Tecnai 12 Transmission Electron Microscope is employed with a Teitz 214 high resolution bottom mounted digital camera.

The objective of the experiments is to examine the competition between MMT concentration, temperature, oxygen and time effects in terms of fundamental processes. The well-characterized boundary conditions and flame structure enable systematic observations that could be explained based

on thermodynamic or kinetics considerations. The thermodynamic framework outlined above is the basis to evaluate nucleation, growth and equilibrium behaviour for the manganese oxides formed. This complementary modelling and experiment approach enables determination of parameters that could be generalized for any synthesis process.

## Results and discussion

Modelling tools are used here to design flame conditions with desired temperature-oxygen-time histories in the post-flame region. Computed flame structures, neglecting precursor doping, are the basis for determining the particle growth environment in the current work. Premixed stagnation flames are steady with a disc-like flame front having a stand-off distance where opposing convective and burning velocities are balanced. The comparison between experimental and computed flame structure is shown in Fig. 3 in terms of recorded flame images and computed 2D contours. Recorded flame images for other flames with and without precursor doping ( $2340$  K  $< T_{f,max} < 2600$  K, B5-B8) are presented in supplementary material. The flame structure is characterized by a pre-flame zone where the velocity and temperature are very close to the inlet boundary conditions. The flame-front is a

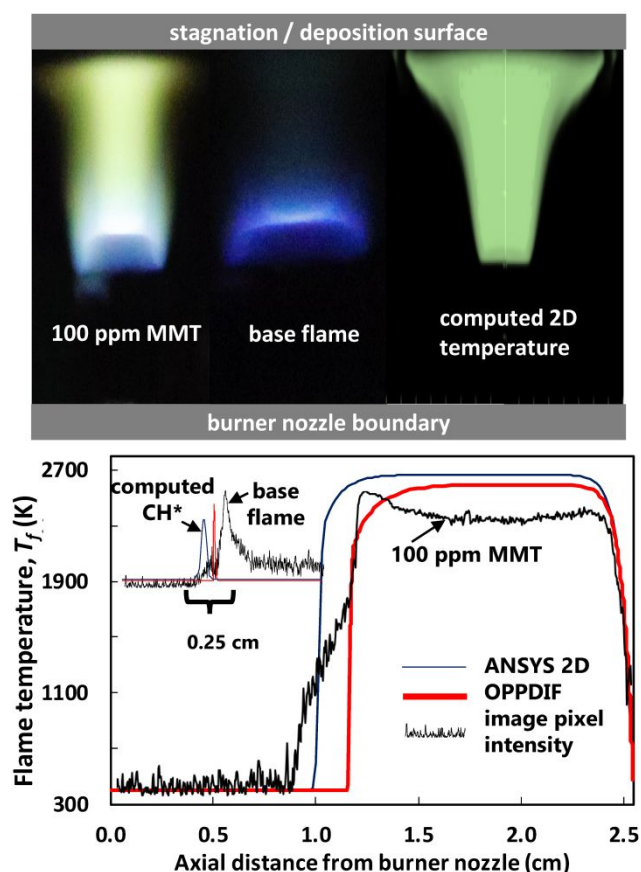


**Figure 3** Comparison between measured and computed flame position in terms of flame images (top-left) and 2D temperature contour computed using ANSYS (top-right). Also shown is comparison between centerline temperature profiles (bottom) and  $CH^*$  concentration profiles (bottom-inset).

narrow region characterized by a sharp jump in temperature and velocity and sharp consumption of fuel and oxygen. The stagnation flame drives a chemical vapor deposition process where precursor decomposes at the flame and undergoes conversion to manganese oxide in the post-flame region.

The flame image shows the MMT doped flame having a post-flame region illuminated by excited Mn oxide species. The illuminated region shifts from light blue next the flame zone to a light green shade which may be an indication of evolving manganese oxide species. The base flame is stabilized in roughly the same position as the precursor doped flame. The position of the 100 ppm of MMT flame is slightly closer to the nozzle boundary which may indicate that this mixture is more reactive than the base flame. This effect may be caused by catalytic behaviour of manganese or by a mixture that is slightly more reactive due to being closer to the stoichiometric ratio. Inspection of the supplementary B series images (Fig. S1) indicates that the flame position is not affected significantly by precursor doping as the largest affect is observed in Fig. 3. The two-dimensional computation of the flame structure shows reasonable agreement to the images in terms of the computed temperature contour. There are instabilities and influences from the environment which result in broadening of the flame position observed in the flame images. A small degree of chemiluminescence appears in a broad region surrounding the MMT doped flame which is caused by radial diffusion, minor flickering and oscillation instabilities.

A comparison in terms of the flame structure at the centerline is also shown in Fig. 3. Measured pixel intensity at the centerline is compared to calculated temperature and CH\* profiles. The doped flame pixel intensity maps out the region of high-temperature emission from manganese oxide species. Without precursor doping, the excited combustion intermediates (i.e CH\*) are the only source of illumination. A comparison between the measured pixel intensity without precursor doping and computed CH\* profiles is shown at the inset. Assuming the measured pixel intensity is due to CH\*, the discrepancy in measured and computed flame position is 0.25 cm for the ANSYS solution. Comparison between the measured pixel intensity and the steep temperature gradient computed by OPPDIF shows good, fortuitous or not, agreement. The flame

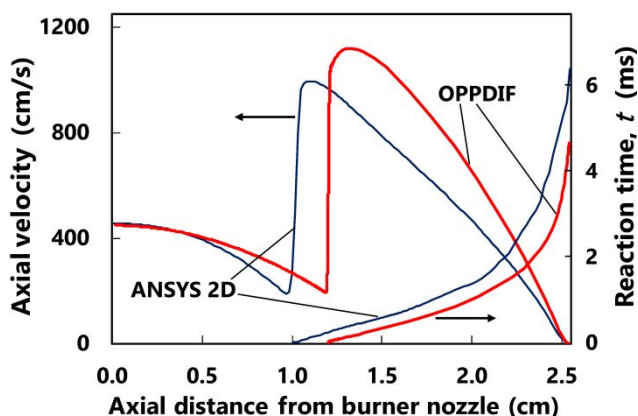


Figure 4 Comparison between typical velocity and reaction time profiles obtained from OPPDIF and ANSYS 2D computations.

temperature gradient predicted by the ANSYS 2D solution lies within 0.15 cm of the doped flame pixel intensity. Both OPPDIF and ANSYS 2D compile USC Mech II in the Chemkin framework with the accompanying thermodynamic and transport models. One difference in the computation is that radiation effects are ignored in the ANSYS workbench and this could explain the higher temperature predicted in the ANSYS computation.

Many two-dimensional flame modelling studies have been carried out to evaluate the optimal counterflow conditions to achieve self-similar conditions.<sup>39</sup> A common focus is the inlet boundary in which plug-flow is important for accurately extrapolating the laminar flame speed from low-strain premixed flames<sup>40</sup>. More careful treatment of the boundary flow profile could extend the range of the self-similar computation for flame extinction<sup>41</sup> and for flames outside of the mixing layer<sup>42</sup>. A typical velocity and reaction time profile is shown in Fig. 4 for both the self-similar (OPPDIF) and two-dimensional (ANSYS) computation. The reaction time applies to Mn oxide synthesis thus the thermophoretic velocity is only added to the convective velocity after the flame front. Higher predicted flame temperature for the two-dimensional calculation has been reported<sup>42,43</sup> and radial momentum and energy equation considerations were shown to become significant for large aspect ratio stagnation configurations<sup>42,44</sup>. These radial uncertainties will be investigated in future work. Overall, the flame position is predicted reasonably well for OPPDIF and ANSYS two-dimensional methods. This comparison indicates that the self-similar assumption taken by OPPDIF provides a fast and accurate computation of the flame structure for a robust range of premixed stagnation flame conditions. Definition of the flame structure enables rigorous determination of the particle trajectory in terms of reaction time. This is especially promising if a quicker method (OPPDIF) could be used to provide insight into the temperature-oxygen-time history during synthesis of manganese oxide and other systems.

The A series of flame synthesis experiments is designed to systematically examine the precursor loading effect isolated

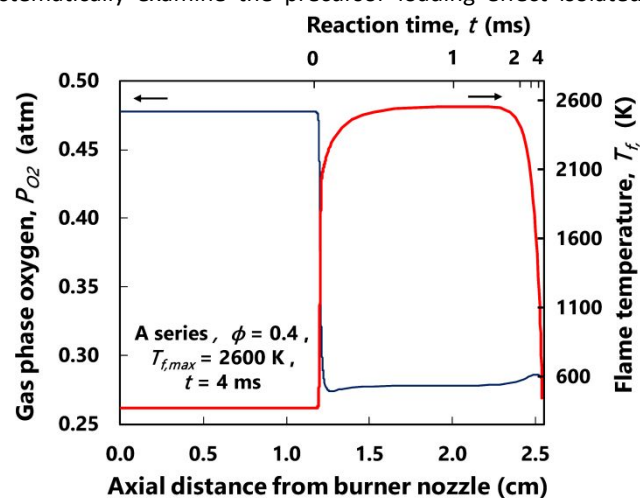
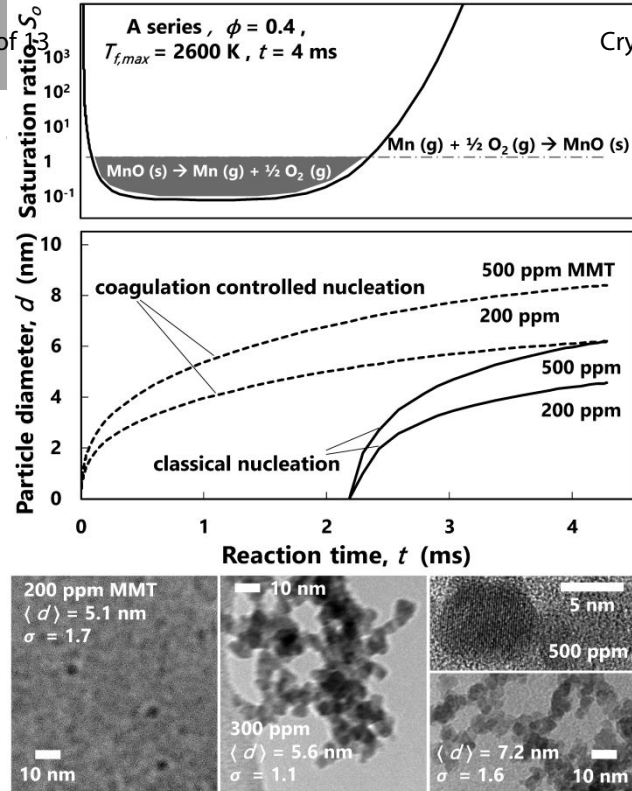


Figure 5 Computed gas phase oxygen and flame temperature profiles obtained with OPPDIF for the A series flame. Also shown is the reaction time computed for manganese oxide formation and growth (top-axis).



**Figure 6** Analysis of nucleation and growth for particles formed in the A Series flame experiments. Saturation ratio profile in terms of reaction time in the flame (top), particle size profile assuming either coagulation controlled or classical nucleation (middle) and TEM images of synthesized nanoparticles (bottom).

from temperature, time and oxygen effects. Flame A ( $\Phi = 0.4$ ,  $T_{f,max} = 2600$  K and  $t = 4$  ms) is examined with 200, 300 and 500 ppm levels of MMT loading. The gas-phase oxygen and temperature profiles computed using the pseudo one-dimensional method (OPPDIF) is shown in Fig. 5 in spatial dimensions. The A flame has a structure characterized by a flame zone positioned  $\sim 1.3$  cm from the burner nozzle with a maximum flame temperature of  $T_{f,max} = 2600$  K. The oxygen flows into the domain at a given partial pressure and gets consumed at the flame front with an excess amount remaining in the post-flame region. The reaction time is calculated from the computed velocity – distance profile. It is assumed that the precursor breaks down to form metallic Mn and the oxidation process begins at the flame front. The top-axis of Fig. 5 shows the translation to reaction time based on these assumptions. As Fig. 5 shows, the manganese oxide spends  $\sim 4$  ms in the post-flame zone of flame A before depositing onto the stagnation surface.

A coagulation-limited nucleation mechanism applies if there is no thermodynamic barrier to manganese oxide condensation. The Kelvin equation has been applied to  $\text{TiO}_2$  in previous reports<sup>45,46</sup> of gas-phase synthesis to determine whether particle nucleation is limited by coagulation. The criterion is that nucleation does not have a thermodynamic barrier if the critical cluster size predicted by the Kelvin equation is smaller than the size of a single oxide molecule<sup>46,47</sup>. In the current study, a similar analysis will be carried out by calculating the saturation ratio for formation of solid MnO from the gas phase (eq. 5) along the computed temperature-oxygen-time history.

The computed saturation ratio – reaction time profile, shown in Fig. 6, indicates that condensation of MnO is not thermodynamically favoured for a significant portion of the flame. Where the Kelvin equation applies ( $S_0 > 1$ ,  $\gamma_{\text{MnO}} = 1.13$  J/m<sup>2</sup>), the predicted critical diameter for stable nuclei is smaller than the MnO monomer size for  $T_f < 1800$  K. This condition occurs at the sharp temperature rise in the flame zone and about 2 ms later as the flame temperature decreases upon approaching the water-cooled stagnation surface. If the thermodynamic barrier exists, particles would nucleate in the flame zone before reaching the maximum flame temperature, then vaporize (or stop growing) at the hottest portion of the flame, then re-condense as the flame temperature cools. Similar behaviour has been reported by Schulz and co-workers in a previous experimental work on synthesis of iron oxide nanoparticles in premixed burner-stabilized flames<sup>33</sup>. Particles were detected by molecular beam mass spectrometry in the flame-front before becoming undetectable at the maximum flame temperature only to reappear in the post-flame region. This observation was rationalized by classical nucleation behaviour. Analysis of the saturation ratio for MnO condensation in the current flame indicates that nucleation could also be governed by a classical mechanism.

For classical nucleation, the size of the final manganese oxide nanoparticles would be smaller than predicted by a coagulation-limited process because the thermodynamic barrier prevents growth for a portion of the reaction time. The particle size is estimated here based on the simplified solution to the coagulation equation:

$$d(t_i) = d_{i-1} (1 + K_{ii} N_{i-1} t_{i-1})^{1/3} \quad (8)$$

where  $t_{i-1}$  is interval between the previous grid point,  $d_{i-1}$  is the particle diameter of the previous grid point,  $N_{i-1}$  is the number density of the previous grid point and  $K_{ii}$  the coagulation coefficient. The coagulation coefficient used here is for collisions of like-sized particles in the free molecular regime:<sup>48</sup>

$$K_{ii} = 4\alpha \left( \frac{6kT d_{i-1}}{\rho_p} \right)^{1/2} \quad (9)$$

where  $\alpha$  is the collision efficiency,  $k$  is the Boltzmann constant,  $T$  is temperature,  $d_{i-1}$  is the particle diameter of the previous grid point and  $\rho_p$  is the bulk density of the oxide. Collision efficiency varies widely in this size range depending on particle size, temperature and material properties but the value was kept at  $\alpha = 0.5$  as a compromise between the range of  $0.1 < \alpha < 0.9$  commonly observed.<sup>48</sup> The coagulation equation was solved in discrete steps based on computed temperature-time history profile grid.

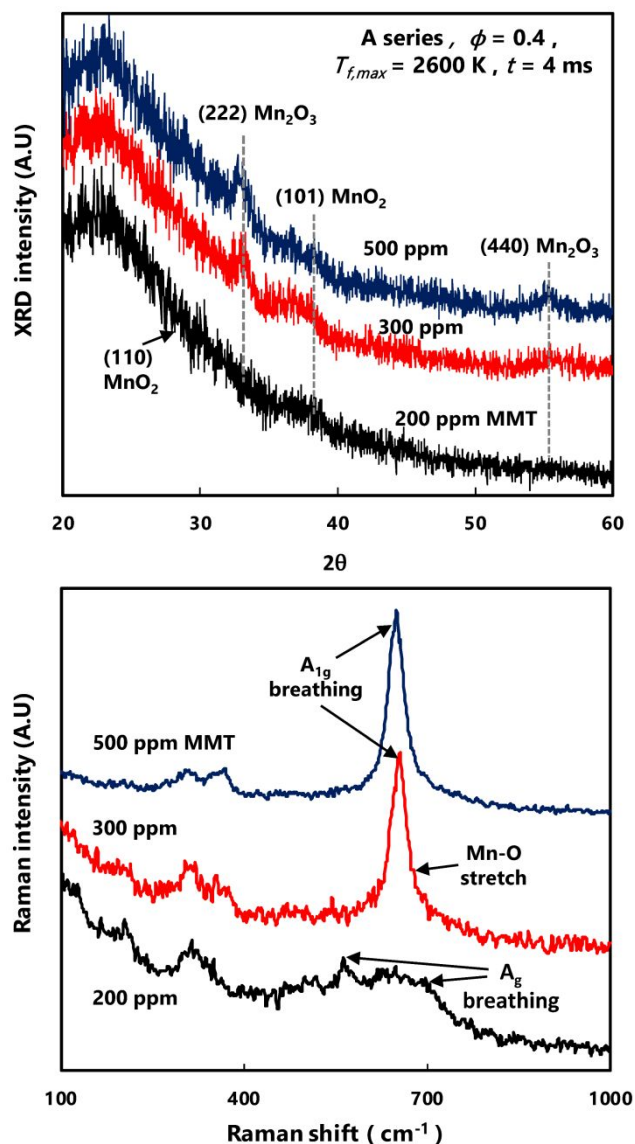


**Figure 7** Characterization of nanocrystalline manganese oxide synthesized in A Series flame experiments. XRD patterns (top) and Raman spectra (bottom) for films deposited with 200 ppm and 500 ppm MMT precursor loading

Two potential scenarios for growth by coagulation are summarized in Fig. 6. Nucleation and growth only limited by coagulation would result in particles with  $d \sim 6$  nm assuming a monomodal size distribution starting at the flame front from 200 ppm of MnO monomer ( $d = 0.34$  nm). The final particles would be  $\sim 2$  nm smaller if growth did not begin until the saturation ratio reached unity in the post-flame region. In the current study, characterization of the particles is only carried out for materials deposited at the stagnation surface. Particle sizing by analysis of the TEM images in ImageJ, also shown in Fig. 6, indicates that the size of particles ranges from 5–7 nm for the conditions studied. The measured particle sizes are significantly smaller than that predicted by the coagulation-limited assumptions taken in Fig. 6. The above analysis is to provide preliminary justification for a classical nucleation mechanism. There are many details required to rigorously quantify the nucleation process. For example, the dependence

of the saturation ratio on conversion of Mn(g) to MnO(s) (plotted as supplementary material) would shift the unity crossover to later reaction time.

Characterization of the final manganese oxide products formed in Flame A is shown in Fig. 7 in terms of XRD and Raman spectroscopy. As expected, X-ray diffraction is not strong for these relatively disordered and ultrafine particles. The most prominent faces were observed on the 500 ppm case as (222) and (440) attributed to Mn<sub>2</sub>O<sub>3</sub>. Faint evidence of MnO<sub>2</sub> peaks appear as (101) and (110) in the lower ppm loading cases. Baseline corrected profiles are also included in the supplementary material. Lattice fringes were detectable by TEM as shown in Fig. 6 for the 500 ppm case. Examination of short range order by Raman spectroscopy shows a more clear evolution at increasing particle loading. The A<sub>1g</sub> breathing mode of Mn oxide octahedra is observed at 650 cm<sup>-1</sup> for materials formed under higher precursor loading (300 and 500 ppm) and this is a characteristic of Mn<sub>3</sub>O<sub>4</sub>. Several studies attribute this to known thermal decomposition behaviour of Mn<sub>2</sub>O<sub>3</sub> under laser power<sup>49,50</sup>. The flame synthesis origin of the manganese oxide may have caused this high-temperature feature to persist in the product structure rather than artifacts from the laser (1 mW). The Mn-O stretch mode is observed at 680 cm<sup>-1</sup> for the 300 and 500 ppm cases which corresponds to Mn<sub>2</sub>O<sub>3</sub><sup>49</sup>. The Raman spectra of the 200 ppm loading case shows a clear departure in that the dominant mode A<sub>1g</sub> is no longer present. Instead, broad A<sub>g</sub> modes are observed above 600 cm<sup>-1</sup> and these have been attributed to disordered MnO<sub>2</sub> structures<sup>50</sup>.

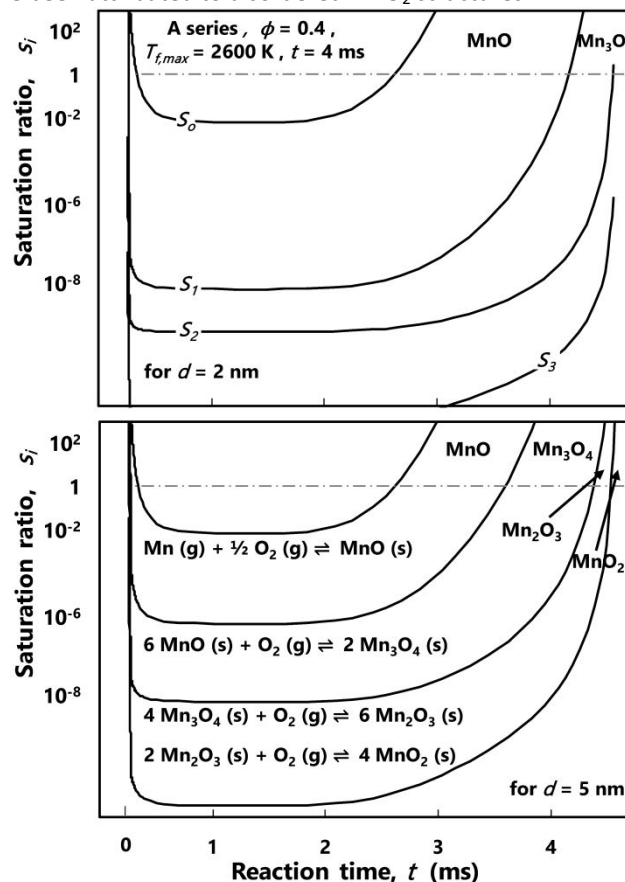


**Figure 8** Analysis of local phase equilibria between manganese oxides with  $d = 2$  nm (top) and  $d = 5$  nm (bottom) in the A series flame in terms of saturation ratio – reaction time profiles.

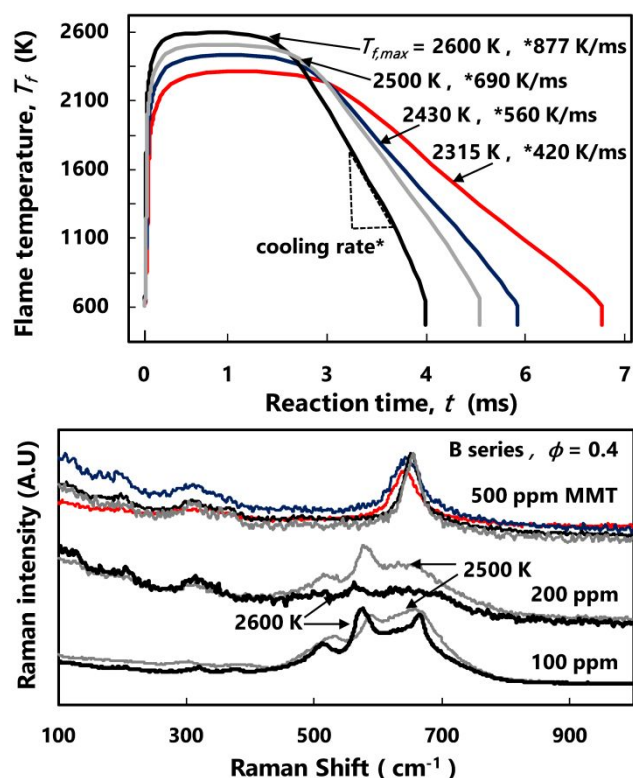


**Figure 9** Temperature – reaction time profiles (top) and Raman spectra for nanocrystalline manganese oxide formed (bottom) in the B Series flame experiments.

For increasing precursor loading in the same oxygen-rich flame, the particle size increases and the manganese oxidation state decreases. This observation may be explained by equilibria between the oxides governed by size, temperature and oxygen partial pressure. The equilibrium conditions are mapped onto reaction time space in Fig. 8 in terms of the saturation ratios of the four manganese oxidation steps (eqs. 1-4). Local temperature and oxygen partial pressure are known as the manganese oxide progresses through the synthesis domain and comparison to the equilibrium condition gives insight into the thermodynamically favoured processes throughout. This analysis is carried out for  $d = 2$  nm and 5 nm to present conditions that overlap all three of the precursor conditions carried out in the A series of experiments. The surface energy effect causes a significant shift in the boundaries shown in Fig. 8 such that  $M_2O_3$  and  $MnO_2$  do not cross the unity saturation threshold for small particle size. If the boundaries shown are accurate, the higher oxidation states are only stable for larger particle sizes in this flame.

The computed saturation ratio profile ignores the minor discrepancy between the measured and computed flame position. The presence of precursor, particles and three-dimensional flow effects are suspected of causing this discrepancy. The stretch effect does not cause a significant deviation from the adiabatic flame temperature for the global strain rates studied here. Computations in the supplementary material (Table S1 and Fig. S2) show, in the absence of particles, the calculated maximum flame temperature is effectively the adiabatic flame temperature and the stretch effect causes a 3%

reduction in temperature in the flame zone for nearly twice the global strain rate. We also assume the computed temperature is not affected by the presence of particles. Flame temperature profiles were measured by thermocouple in previous reports on  $TiO_2$  nanoparticle synthesis in stagnation flames<sup>13,51</sup>. The particle concentration was in the same range as the current study and the high-temperature emissivity is on the order of 0.5 for both  $Mn_3O_4$  and  $TiO_2$ .<sup>52</sup> Therefore, any effect of particle radiation is expected to be similar for the current manganese oxide flames. Measured temperatures were 40 K to 100 K lower than the adiabatic flame temperature in the  $TiO_2$  synthesis flames depending on particle loading. Pratsinis and co-workers measured the flame temperature for  $TiO_2$  synthesis in premixed flames as well but temperature was only 200 K higher than the un-doped flame even with two orders of magnitude greater precursor loading.<sup>53</sup> To account for the current uncertainty in the temperature due to particles, the saturation profile was calculated for a range of temperature  $\pm 100$  K from the original OPPDIF computation (supplementary Fig S4). The range of saturation ratios changes moderately with temperature and the  $\pm 13$  % shift in boundaries does not alter the conclusions drawn.

The saturation ratio leading to  $Mn_2O_3$  and  $MnO_2$  phases are predicted to reach  $S > 1$  when  $d > 5$  nm. The thermodynamically predicted phase for the collected material is  $MnO_2$  because the particles collected are  $> 5$  nm and the final synthesis temperature is on the low range of the phase diagram. Characterization of the oxide products discussed above indicates that signatures of  $Mn_3O_4$ ,  $Mn_2O_3$  and  $MnO_2$  are present depending on the level of precursor loading. This may indicate that phase equilibrium is only achieved when the particles are small enough to equilibrate on the millisecond timescale. The  $Mn_2O_3$  and  $Mn_3O_4$  features observed may be metastable characteristics which formed at higher temperature and were quenched as the particles deposited.

Temperature and precursor loading effects are explored further in the B series of flame experiments. The series is a set of flames with  $\Phi = 0.4$  having comparable reaction times at increasing flame temperatures ( $2315 \text{ K} < T_{f,max} < 2600 \text{ K}$ ). The computed flame temperature-reaction time profiles based on the pseudo one-dimensional formulation is shown in Fig. 9. Images of these flames with and without precursor loading are shown in supplementary material. The flame images show that

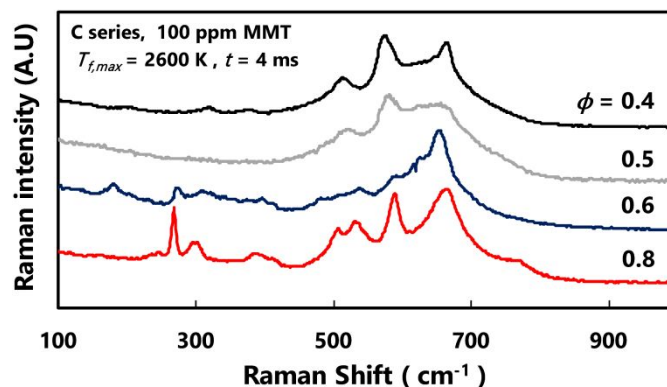


**Figure 10** Raman spectra for nanocrystalline manganese oxide formed in the C Series flame experiments

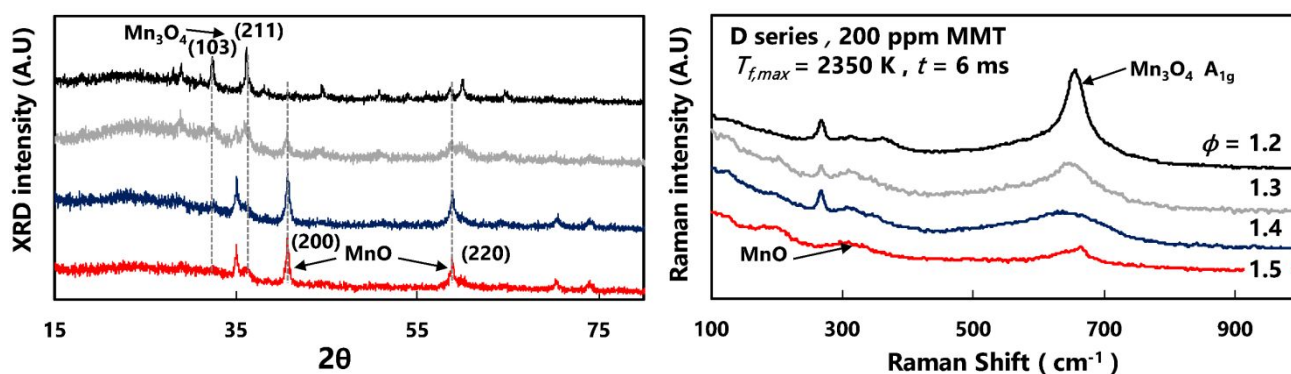


**Figure 11** Characterization of nanocrystalline manganese oxide synthesized in the D Series flame experiments. XRD patterns (left) and Raman spectra (right) for materials deposited from the flame.

the position of the flame does not change significantly due to the presence of MMT precursor. In addition, the position of the flame varies in order to keep the reaction time comparable for the given range of flame temperatures. By expressing the synthesis region in terms of reaction time, the systematic comparison of flame structure shown in Fig. 9 could be carried out. The computed flame structures show that the series also provides insight into the cooling rate effect as the hottest flame approaches the stagnation surface with twice the cooling rate as the coldest flame in the series. The cooling rate is expected to provide another means to control the properties of the material formed.

A summary of products formed in the B series is also shown in Fig. 9 in terms of Raman spectra. The spectra show the oxide formed does not depend on the temperature and cooling rate for the 500 ppm precursor loading condition. Features of  $\text{Mn}_2\text{O}_3$  products are observed for 500 ppm MMT loading at all temperature conditions. If the equilibrium considerations discussed above hold,  $\text{MnO}_2$  should be the thermodynamically favoured phase due to the final size and synthesis temperature. Similar to the A series, the observed  $\text{Mn}_2\text{O}_3$  products may be a metastable phase that is too massive to equilibrate even at a reduced cooling rate. The spectra corresponding to  $\text{Mn}_2\text{O}_3$  is observed for the largest particles across a temperature range of 300 K and cooling rates spanning 400 K / ms. This is contrasted to the spectra for the lower ppm conditions of the same flames. Manganese oxides forming in the 100 and 200 ppm loading cases have Raman features corresponding to  $\text{MnO}_2$  structures. The spectra attributed to products formed at the 100 ppm condition show signatures of the  $\text{MnO}_6$  octahedra stretch modes corresponding to pyrolusite  $\text{MnO}_2$ <sup>50</sup>. Pyrolusite is considered a relatively ordered  $\text{MnO}_2$  structure and other  $\text{MnO}_2$  structures have been characterized by degrees of pyrolusite intergrowth. The spectra observed for the 200 ppm cases may be described as  $\text{MnO}_2$  with varying pyrolusite components<sup>50</sup> which, under the given cooling rate, did not fully become an ordered structure. Examination of competing particle growth and oxidation effects carried out in the A and B series of flame experiments shows both metastable and thermodynamically favoured phases could be obtained depending on the details of the temperature-oxygen-time history during synthesis.

The role of gas-phase oxygen is further examined for low precursor loading (100 ppm) in the C series of flame experiments ( $0.4 < \Phi < 0.8$ ). The flames are designed to have comparable temperature-time history while decreasing the partial pressure of oxygen during synthesis. Characterization of the final products is shown in Fig. 10 in terms of Raman spectra. The  $\Phi = 0.4$  spectrum is characteristic to pyrolusite  $\text{MnO}_2$ <sup>50</sup>. As the series progresses to lower oxygen growth conditions, features of the Raman spectra appear to evolve from  $\text{MnO}_2$  to  $\text{Mn}_2\text{O}_3$ . The variety of peaks observed from 500-700  $\text{cm}^{-1}$  have been attributed to pyrolusite  $\text{MnO}_2$  (with various degrees of pyrolusite (order)<sup>50</sup>). At  $\Phi = 0.8$ , features of  $\text{Mn}_2\text{O}_3$  appear in terms of new low wavenumber features and a prominent  $A_{1g}$  breathing mode. Series C flame experiments demonstrate the role of gas-phase oxygen in tuning the properties of the deposited manganese oxide for a given size range and temperature-time history.

Oxygen-lean growth conditions were also examined to observe the formation of lower manganese oxidation states in series D flame experiments. Flames having  $1.2 < \Phi < 1.5$  were studied with comparable temperature-time history. Characterization of the products formed in these flames is shown in Fig. 11 in terms of XRD and Raman spectra. The formation of  $\text{MnO}$  is observed, for the first time by flame synthesis, in the most oxygen lean flame ( $\Phi = 1.5$ ). The XRD and Raman features show a systematic evolution from  $\text{Mn}_3\text{O}_4$  products to  $\text{MnO}$  products as the equivalence ratio is increased (gas-phase  $\text{O}_2$  decreases). A range of titanium oxide structures was reported for increasing equivalence ratio<sup>12</sup> but a range of metal oxide valence this extensive has never been reported.

Manipulation of  $\text{O}_2$  during particle growth was systematically carried out in the C and D series of flame experiments to observe the role of gas-phase oxygen on resulting particle oxidation state / structure. Complementary experimental and modelling studies in the premixed stagnation flame configuration enables systematic study of competing thermodynamic and kinetic processes. Computed oxygen partial pressure - reaction time profiles are shown in Fig. 12 for the D series of flames. As the computed oxygen profiles show, manganese oxide forms under similar flame structure with oxygen being the only variation across the flames. The oxygen present in the post-flame region is much lower than the oxygen-

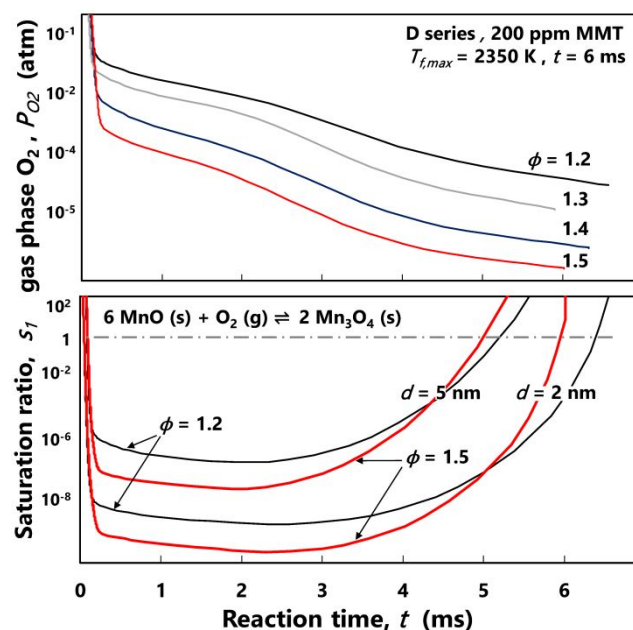


**Figure 12** Computed oxygen partial pressure -reaction time profiles for the D series (top) and saturation ratio ( $S_1$ )-reaction time profiles (bottom) for selected conditions and particle size.

rich flames studied above and this enables products having lower oxidation states to be favoured. The given range of  $\Phi$  examined in the D series results in oxygen partial pressures spanning an order of magnitude relative to each other.

The saturation ratio for MnO-Mn<sub>3</sub>O<sub>4</sub> equilibrium ( $S_1$ ) is also mapped to the reaction time in Fig. 12 for the  $\Phi = 1.2$  and 1.5 cases. For early growth stages (i.e.  $d = 2$  nm) the window for Mn<sub>3</sub>O<sub>4</sub> stability is narrow. As the particle grows, the surface energy effect widens the Mn<sub>3</sub>O<sub>4</sub> stability zone for both flames. The saturation ratio analysis carried out here does not account for the oxygen consumed by the manganese during oxidation to MnO and Mn<sub>3</sub>O<sub>4</sub>. At these trace oxygen levels, the saturation ratios may actually cross the unity threshold later due to oxygen partial pressure lower than computed for the flame structure. This effect may be more pronounced in the most fuel lean case ( $\Phi = 1.5$ ) where the saturation ratio is an order of magnitude lower at the highest flame temperature. Nonetheless, the current analysis shows that the lower oxides (MnO and Mn<sub>3</sub>O<sub>4</sub>) are thermodynamically favoured in oxygen-lean flame synthesis conditions.

## Conclusions

Formation of nanocrystalline manganese oxide nanoparticles in premixed stagnation flames was systematically examined. Comparisons among flame structure computations and experimentally determined flame position indicates that a pseudo one-dimensional model performs reasonably well for characterizing the structure of the synthesis domain. With the temperature-oxygen-time history defined, thermodynamic analysis was carried out by comparing local conditions to

equilibrium values. Analysis of the saturation ratio for formation of condensed MnO in the flame indicates that nucleation may be limited by a thermodynamic barrier. This nucleation mechanism is supported by measured particle sizes smaller than what would be expected from a coagulation limited growth process.

Manganese oxide nanoparticles having II, II-III, III or IV oxidation states were observed depending on the flame conditions. Size-dependent equilibrium for oxygen partial pressure was compared to the computed local concentration to assess thermodynamically favored conditions. An oxygen-rich flame was examined with increasing particle loading (A series) and the thermodynamically favored product, MnO<sub>2</sub>, was obtained only for the smallest particle size. Further examination of oxygen-rich conditions with a range of temperatures and cooling rates (B series) showed that phase equilibrium may not be achieved for larger particle sizes due to longer times required for thermal equilibration. Nanocrystalline MnO, reported here for the first time by flame synthesis, was obtained in oxygen lean flames. Observations of manganese oxide formation under a range of oxygen conditions (C and D series) showed that the oxide phase produced could be tuned to some extent. Overall, definition of the temperature-oxygen-time history and size-dependent equilibria enable production of nanocrystalline manganese oxide with a range of properties.

## Conflicts of interest

There are no conflicts to declare

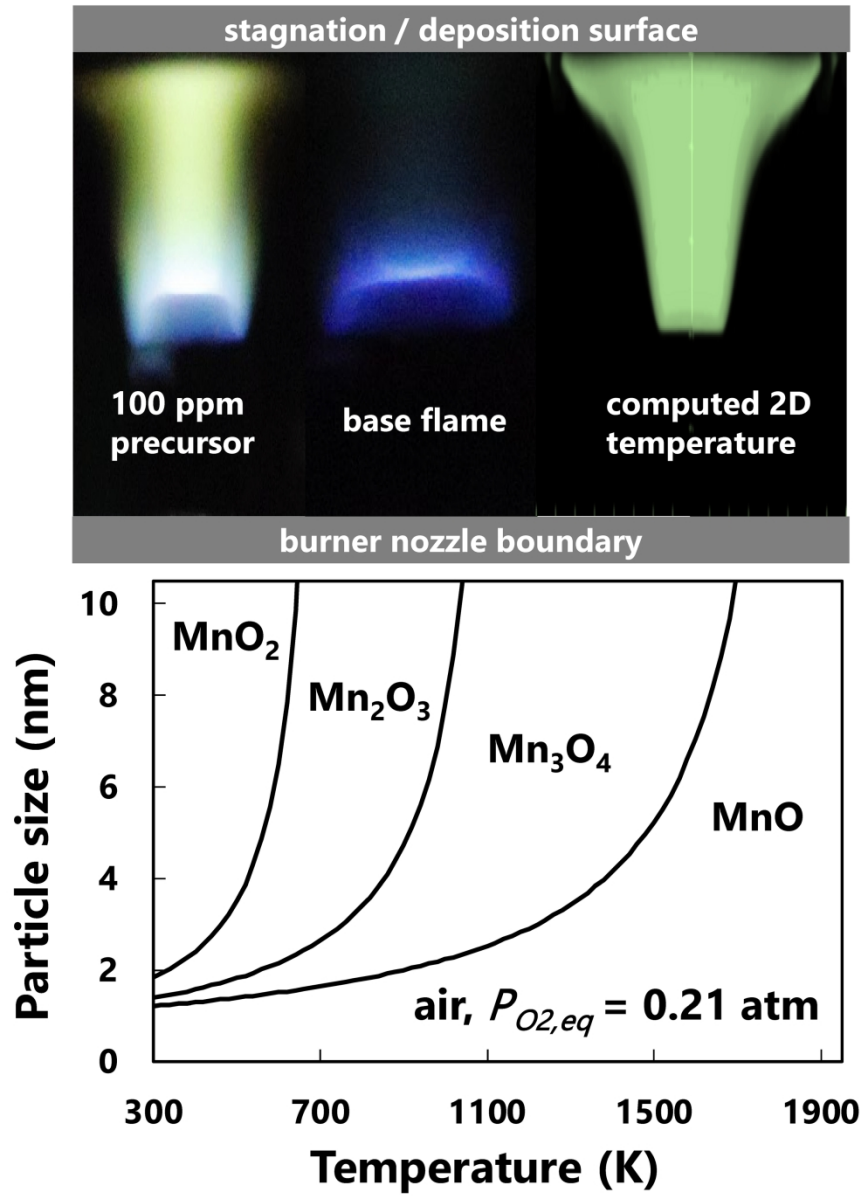
## Acknowledgements

The work was supported by NSF Combustion and Fire Systems program under Award 1841357. Prof. David Pullman (SDSU Chemistry) and Dr. Ingrid Neisman (SDSU Microscopy Center) are gratefully acknowledged for assistance in nanoparticle characterization.

## References

- 1 W. Wei, X. Cui, W. Chen and D. G. Ivey, *Chem. Soc. Rev.*, 2011, **40**, 1697–1721.
- 2 M. M. Thackeray, C. S. Johnson, J. T. Vaughey, N. Li and S. A. Hackney, *J. Mater. Chem.*, 2005, **15**, 2257–2267.
- 3 J. Shin, R. M. Anisur, M. K. Ko, G. H. Im, J. H. Lee and I. S. Lee, *Angew. Chemie Int. Ed.*, 2009, **48**, 321–324.
- 4 K. M. L. Taylor, W. J. Rieter and W. Lin, *J. Am. Chem. Soc.*, 2008, **130**, 14358–14359.
- 5 C. Liu, J.-W. Shi, C. Gao and C. Niu, *Appl. Catal. A Gen.*, 2016, **522**, 54–69.
- 6 M. Kang, E. D. Park, J. M. Kim and J. E. Yie, *Appl. Catal. A Gen.*, 2007, **327**, 261–269.
- 7 M. Wiechen, M. M. Najafpour, S. I. Allakhverdiev and L. Spiccia, *Energy Environ. Sci.*, 2014, **7**, 2203–2212.
- 8 T. J. Patey, R. Buchel, S. H. Ng, F. Krumeich, S. E. Pratsinis

- and P. Novak, *J. Power Sources*, 2009, **189**, 149–154.
- 9 F. O. Ernst, H. K. Kammler, A. Roessler, S. E. Pratsinis, W. J. Stark, J. Ufheil and P. Novak, *Mater. Chem. Phys.*, 2007, **101**, 372–378.
- 10 S. Li, Y. Ren, P. Biswas and S. D. Tse, *Prog. Energy Combust. Sci.*, 2016, **55**, 1–59.
- 11 J. Camacho, C. Liu, N. Montes and H. Wang, *9th U. S. Natl. Combust. Meet.*, 2015, 2B09.
- 12 M. Y. Manuputty, J. A. H. Dreyer, Y. Sheng, E. J. Bringley, M. L. Botero, J. Akroyd and M. Kraft, *Chem. Sci.*, 2019, **10**, 1342–1350.
- 13 B. Zhao, K. Uchikawa, J. R. McCormick, C. Y. Ni, J. G. Chen and H. Wang, *Proc. Combust. Inst.*, 2005, **30**, 2569–2576.
- 14 C. Liu, J. Camacho and H. Wang, *ChemPhysChem*, 2018, **19**, 180–186.
- 15 R. J. Kee, J. A. Miller, G. H. Evans and G. Dixon-Lewis, *Symp. Combust.*, 1989, **22**, 1479–1494.
- 16 K. Seshadri and F. A. Williams, *Int. J. Heat Mass Transf.*, 1978, **21**, 251–253.
- 17 J. M. Bergthorson, S. D. Salusbury and P. E. Dimotakis, *J. Fluid Mech.*, 2011, **681**, 340–369.
- 18 C. Houtman, D. B. Graves and K. F. Jensen, *J. Electrochem. Soc.*, 1986, **133**, 961–970.
- 19 S. Memarzadeh, E. D. Tolmachoff, D. J. Phares and H. Wang, *Proc. Combust. Inst.*, 2011, **33**, 1917–1924.
- 20 H. Zhang and J. F. Banfield, *J. Mater. Chem.*, 1998, **8**, 2073–2076.
- 21 N. Birkner and A. Navrotsky, *Am. Mineral.*, 2012, **97**, 1291–1298.
- 22 V. Bayer, C. Franchini and R. Podlucky, *Phys. Rev. B*, 2007, **75**, 35404.
- 23 A. E. Lutz, R. J. Kee, J. F. Grcar and F. M. Rupley, 1997.
- 24 R. J. Kee, F. M. Rupley and J. A. Miller, 1989.
- 25 H. Wang, X. You, A. V. Joshi, S. G. Davis, A. Laskin, F. Egolfopoulos and C. K. Law, [http://ignis.usc.edu/USC\\_Mech\\_II.htm](http://ignis.usc.edu/USC_Mech_II.htm).
- 26 J. Camacho, A. V. Singh, W. Wang, R. Shan, E. K. Y. Yapp, D. Chen, M. Kraft and H. Wang, *Proc. Combust. Inst.*, 2017, **36**, 1001–1009.
- 27 E. K. Y. Yapp, D. Chen, J. Akroyd, S. Mosbach, M. Kraft, J. Camacho and H. Wang, *Combust. Flame*, 2015, **162**, 2569–2581.
- 28 A. D. Abid, J. Camacho, D. A. Sheen and H. Wang, *Combust. Flame*, 2009, **156**, 1862–1870.
- 29 J. Bonpua, Y. Yagües, A. Aleshin, S. Dasappa and J. Camacho, *Proc. Combust. Inst.*, 2019, **37**, 943–951.
- 30 I. Wlokas, A. Faccinetto, B. Tribalet, C. Schulz and A. Kempf, *Int. J. Chem. Kinet.*, 2013, **45**, 487–498.
- 31 J. Z. Wen, C. F. Goldsmith, R. W. Ashcraft and W. H. Green, *J. Phys. Chem. C*, 2007, **111**, 5677–5688.
- 32 O. M. Feroughi, S. Hardt, I. Wlokas, T. Hülser, H. Wiggers, T. Dreier and C. Schulz, *Proc. Combust. Inst.*, 2015, **35**, 2299–2306.
- 33 S. Kluge, L. Deng, O. Feroughi, F. Schneider, M. Poliak, A. Fomin, V. Tsionsky, S. Cheskis, I. Wlokas, I. Rahinov, T. Dreier, A. Kempf, H. Wiggers and C. Schulz, *CrystEngComm*, 2015, **17**, 6930–6939.
- 34 A. Matraszek, M. Miller, L. Singheiser and K. Hilpert, *J. Eur. Ceram. Soc.*, 2004, **24**, 2649–2656.
- 35 A. Navrotsky, C. Ma, K. Lilova and N. Birkner, *Science (80-. )*, 2010, **330**, 199 LP – 201.
- 36 J. M. Bergthorson, California Institute of Technology, 2005.
- 37 E. Meeks, R. J. Kee, D. S. Dandy and M. E. Coltrin, *Combust. Flame*, 1993, **92**, 144–160.
- 38 N. G. Glumac and D. G. Goodwin, *Mater. Lett.*, 1993, **18**, 119–122.
- 39 C. S. Lindberg, M. Y. Manuputty, P. Buerger, J. Akroyd and M. Kraft, *J. Aerosol Sci.*, 2019, **138**, 105451.
- 40 V. Mittal, H. Pitsch and F. Egolfopoulos, *Combust. Theory Model.*, 2012, **16**, 419–433.
- 41 U. Niemann, K. Seshadri and F. A. Williams, *Combust. Flame*, 2015, **162**, 1540–1549.
- 42 R. F. Johnson, A. C. VanDine, G. L. Esposito and H. K. Chelliah, *Combust. Sci. Technol.*, 2015, **187**, 37–59.
- 43 T. Yuan, Y.-H. Lai and C.-K. Chang, *Combust. Flame*, 2008, **154**, 557–568.
- 44 N. Bouvet, D. Davidenko, C. Chauveau, L. Pillier and Y. Yoon, *Combust. Flame*, 2014, **161**, 438–452.
- 45 G. D. Ulrich, *Combust. Sci. Technol.*, 1971, **4**, 47–57.
- 46 Y. Xiong and S. E. Pratsinis, *J. Aerosol Sci.*, 1991, **22**, 637–655.
- 47 T. Kodas and M. Hampden-Smith, *Aerosol Processing of Materials*, Wiley-VCH, 1999.
- 48 S. K. Friedlander, *Smoke, Dust, and Haze: Fundamentals of Aerosol Behavior*, Oxford University Press, New York, 2000.
- 49 F. Buciuman, F. Patcas, R. Craciun, D. R. T. Zahn and D. R. T. Zahn, *Phys. Chem. Chem. Phys.*, 1999, **1**, 185–190.
- 50 C. Julien, M. Massot, S. Rangan, M. Lemal and D. Guyomard, *J. Raman Spectrosc.*, 2002, **33**, 223–228.
- 51 E. D. Tolmachoff, A. D. Abid, D. J. Phares, C. S. Campbell and H. Wang, *Proc. Combust. Inst.*, 2009, **32**, 1839–1845.
- 52 G. K. Burgess and R. G. Waltenberg, *Phys. Rev.*, 1914, **4**, 546–547.
- 53 O. I. Arabi-Katbi, S. E. Pratsinis, P. W. Morrison and C. M. Megaridis, *Combust. Flame*, 2001, **124**, 560–572.



106x147mm (600 x 600 DPI)